

Chemistry and Properties of Medium-Mn Two-Stage TRIP Steels



DANIEL M. FIELD, JINGJING QING, and DAVID C. VAN AKEN

Eight medium manganese steels ranging from 10 to 15 wt pct Mn have been produced with varying levels of aluminum, silicon, and carbon to create steels with varying TRIP (transformation-induced plasticity) character. Alloy chemistries were formulated to produce a range of intrinsic stacking fault energies (ISFE) from -2.2 to 13.3 mJ/m² when calculated at room temperature for an austenitic microstructure having the nominal alloy composition. Two-stage TRIP behavior was documented when the ISFE of the γ -austenite phase was 10.5 mJ/m² or less, whereas an ISFE of 11.9 mJ/m² or greater exhibited TWIP (twin-induced plasticity) with single-stage TRIP to form α -martensite. Properties were measured in both hot band (hot rolled) and batch annealed (hot rolled, cold rolled, and annealed) conditions. Hot band properties were influenced by the Si/Al ratio and this dependence was related to incomplete recovery during hot working for alloys with Si/Al ratios greater than one. Batch annealing was conducted at 873 K (600 °C) for 20 hours to produce ultrafine-grained microstructures with mean free slip distances less than 1 μ m. Batch-annealed materials were found to exhibit a Hall–Petch dependence of the yield strength upon the mean free slip distance measured in the polyphase microstructure. Ultimate tensile strengths ranged from 1450 to 1060 MPa with total elongations of 27 to 43 pct. Tensile ductility was shown to be proportional to the sum of the products of volume fraction transformed times the volume change associated for each martensitic transformation. An empirical relationship based upon the nominal chemistry was derived for the ultimate tensile strength and elongation to failure for these batch-annealed steels. Two additional alloys were produced based upon the developed understanding of these two-stage TRIP steels and tensile strengths of 1150 MPa with 58 pct total elongation and 1400 MPa and 32 pct ductility were achieved.

<https://doi.org/10.1007/s11661-018-4798-6>

© The Minerals, Metals & Materials Society and ASM International 2018

I. INTRODUCTION

A. Design and Processing of 3rd Generation Advanced High-Strength Steels

MICROSTRUCTURAL engineering is central to the development of 3rd generation advanced high-strength steel for automotive application. Quench and partitioning of martensitic steels is an established approach to obtain the desired combination of α -martensite and γ -austenite with partitioning of carbon to stabilize the γ -austenite at room temperature. Transformation-induced plasticity (TRIP) in quench and partitioned steel results from the transformation of γ -austenite to α -martensite, which results in both greater formability

and improved crashworthiness. Quench and Partitioning steels exhibit ultimate tensile strengths in excess of 1500 to 1700 MPa and elongations to failure of 20 to 10 pct.^[1–3]

Medium manganese (5 to 12 wt pct Mn) steels are also potential 3rd generation advanced high-strength steels where fine-grained microstructures of α -ferrite and γ -austenite are created by first cold working and isothermal annealing. Partitioning of substitutional alloying elements (*e.g.*, Al, Mn) and interstitial carbon stabilize the γ -austenite, *i.e.*, Al is partitioned to the α -ferrite for solid solution strengthening and Mn and C are partitioned to the γ -austenite to produce TRIP during straining. TRIP behavior may be preceded by twin-induced plasticity (TWIP) or may exhibit two-stage TRIP where γ -austenite first transforms to ϵ -martensite and subsequently transforms to α -martensite. These medium-Mn steels demonstrate ultimate tensile strengths ranging from 700 to 1550 MPa and total elongations of 65 to 10 pct.^[4–9]

Processing of medium manganese steels includes hot rolling to form a hot band thickness of 1.8 to 3.3 mm,^[10]

DANIEL M. FIELD, JINGJING QING, and DAVID C. VAN AKEN are with the Department of Materials Science and Engineering, Missouri University of Science and Technology Rolla, MO 65409. Contact e-mail: dfb52@mst.edu

Manuscript submitted date January 16, 2018.

Article published online July 13, 2018

cold rolling the hot band, and intercritical annealing within a temperature range of 873 K to 1023 K (600 °C to 750 °C) to obtain a metastable γ -austenite that TRIP's to α -martensite. The stability and volume fraction of retained γ -austenite is controlled by the time and temperature at which annealing is performed. Zhang *et al.*^[11] investigated a 7 wt pct Mn steel annealed at 893 K (620 °C) for times ranging from 3 minutes to 96 hours and found that the increased time at temperature coarsened the γ -austenite from 300 to 940 nm, but noted that the volume fraction of γ -austenite was relatively constant at \sim 40 vol pct. During tensile testing, the γ -austenite transformed to α -martensite. Luo *et al.* reported^[12] on two 5 wt pct Mn steels where the intercritical annealing temperature was varied to manipulate the Mn and C content of the γ -austenite. A maximum in the measured retained γ -austenite at ambient temperature was obtained by intercritical annealing at 943 K (670 °C) for 10 minutes. Zhang *et al.*^[13] investigated a 0.2 C to 5 Mn (in wt pct.) steel hot worked at an unspecified temperature, annealed at 923 K (650 °C) for 12 hours to fully recrystallize the microstructure and upon cooling a lath martensite with γ -austenite formed between the laths was observed. The steel was subsequently warm rolled at a subcritical temperature of 923 K (650 °C) with increasing reduction ratios from 0 to 77 pct. They showed that finer lath spacing was obtained with increasing rolling strains, and the lath thickness was decreased from 0.6 to 0.2 μm with respective yield strengths of 490 to 980 MPa.

A distinction between TWIP and TRIP is often generalized by calculation of the intrinsic stacking fault energy (ISFE) of the γ -austenite.^[14–17] There have been many works to determine the ISFE range at which the formation of ε -martensite will transition to mechanical twinning. For intrinsic stacking fault energies \geq 20 mJ/m², alloys will mechanically twin and no ε -martensite is observed. The works by Remy and Pineu,^[15] Allain *et al.*^[16] and Lee *et al.*^[17] showed that in the range of 12 to 17 mJ/m² both mechanical twins and ε -martensite form simultaneously. These works also show that for alloys formulated with calculated ISFE \leq 12 mJ/m², the γ -austenite will transform to ε -martensite without twin formation.

TWIP combined with subsequent TRIP behavior has been observed in alloys formulated such that the room temperature intrinsic stacking fault energy of the γ -austenite is $<$ 15 mJ/m².^[9,18,19] Grässel *et al.*^[19] investigated high manganese ($>$ 15 wt pct) steels with varying levels of silicon and aluminum. They concluded that when the TRIP effect was activated, the tensile strength was increased by as much as 180 MPa as a result of delayed necking to greater uniform strains. Song *et al.*^[18] examined a lightweight duplex steel with composition of 0.3C-6Mn-5Al-bal Fe (in wt pct) with bands of δ -ferrite; after processing the γ -austenite decomposed to a combination of α -ferrite, α -martensite, and γ -austenite. The unstrained γ -austenite contained annealing twins, but deformation bands formed when plastically strained with α -martensite forming by TRIP within deformation twins, producing a combined TWIP–TRIP behavior. Lee *et al.*^[13] showed that for a

TWIP–TRIP steel, the α -martensite that formed during tensile loading occurred at the intersection of TWIP deformation bands. In the work by Lee *et al.*,^[13] a set of constitutive models were developed using nano-indentation to determine the strength of the γ -austenite and the annealed α -ferrite. A Hall–Petch relationship for the yield strength is shown as Eq. [1], where the grain hardening term, k , is 332 MPa $\sqrt{\mu\text{m}}$ and the frictional stress, σ_0 , is 223 MPa.

$$\sigma_{\text{yield}} \text{ (MPa)} = \frac{332 \text{ (MPa}\sqrt{\mu\text{m}})}{\sqrt{D(\mu\text{m})}} + 223 \text{ (MPa)} \quad [1]$$

De Cooman *et al.*^[20] studied a 7 wt pct Mn steel that was intercritically annealed at 873 K and 923 K (600 °C and 650 °C) for 168 hours to produce a dual-phase α + γ ultrafine grain microstructure with the γ -austenite having an intrinsic stacking fault energy reported to be $-$ 5 mJ/m² and $-$ 14 mJ/m². The resultant γ -austenite was shown through TEM analyses to contain both ε -martensite and α -martensite. De Cooman states that the α -martensite always nucleated within the ε -martensite. Recent developments with cold working followed by annealing of the two-stage TRIP steels at 873 K (600 °C) produce nanocrystalline grain structures have shown promise in increasing the yield strength up to 830 MPa.^[21,22]

Shape memory Fe–Mn alloys also show a sequential martensitic transformation if strained beyond the elastic limit to produce unrecoverable strain. Both Huang *et al.*^[23] and Shin *et al.*^[24] have reported that strains greater than 4 pct will inhibit the shape memory recovery and it was found that the 4 pct strain correlated closely to the formation of α -martensite within intersecting ε -martensite bands as observed using transmission electron microscopy.^[23,24] Both the shape memory alloys^[23–25] and the earlier work of McGrath *et al.* proposed that the transformation to ε -martensite may occur at stresses below 300 MPa when the γ -austenite grain size is 30 to 100 μm . It should be noted that the ε -martensite is a more densely close-packed structure than γ -austenite and the transformation strain during initial ε -martensite formation may help induce α -martensite upon further straining. A significant volume expansion on the order of 2.2 pct occurs when ε -martensite transforms to α -martensite during Stage II TRIP.^[26]

Two-stage TRIP behavior has been quantitatively followed using interrupted tensile testing and X-ray diffraction to characterize the strain-dependent behavior and microstructural evolution.^[21,25] At strains less than 4 pct (strains up to 10 pct if yield point elongation is observed), the γ -austenite first transforms to ε -martensite and segments the γ -austenite into smaller volumes. The two-stage ($\gamma \rightarrow \varepsilon \rightarrow \alpha$) transformation-induced plasticity (TRIP) behavior^[21,22,25,27,28] is most often observed when the carbon content of the γ -austenite is held below 0.2 wt pct and alloying or partitioning of the γ -austenite produces an intrinsic stacking fault energy below 12 mJ/m².^[14–17] Microstructural refinement observed in these two-stage TRIP alloys is thought to

be responsible for the high work hardening rates, high tensile strengths (> 1200 MPa), and elongations to failure, in excess of 25 pct.

B. Stacking Fault Energy

Mechanical twins and ε -martensite are both formed by the motion of partial dislocations in the γ -austenite to create stacking faults and as shown above TWIP and TRIP can be differentiated by ISFE. The importance of Mn as a major component in TWIP and TRIP steels has been demonstrated by first-principle calculations of both the unstable stacking fault and intrinsic stacking fault energies as discussed by Medvedeva *et al.*^[29] and Limmer *et al.*^[30] A generalized stacking fault energy curve is shown in Figure 1. Stacking faults are produced by shearing the fcc crystal on $\{111\}_\gamma$ in the direction of $\langle 112 \rangle$. An unstable stacking fault is produced by “ $\frac{a}{12} \langle 112 \rangle$ ” or half the displacement of a Shockley partial dislocation. The resultant deformed crystal is typically at a higher energy and represents an unstable configuration. The unstable stacking fault energy represents the barrier to nucleation of a Shockley partial dislocation. Displacing the crystal by a full partial dislocation leads to the formation of an intrinsic stacking fault. Creation of a $\{111\}_\gamma$ stacking fault changes the ABCABC stacking to an AB[CA|CA]BC where the stacking fault is seen as the break line, |, and the portion within the brackets represents four layers of $\{0001\}_\varepsilon$ hcp crystal. Quite often the resultant intrinsic stacking fault energy at room temperature is negative (more stable than the fcc crystal structure) but is still unstable with respect to either the bcc crystal structure or α -martensite. Medvedeva *et al.*^[29] demonstrated a parabolic minimum at 12 atomic percent manganese for the ISFE provided the manganese resides at the stacking fault, whereas there is a continuous decrease in the USFE with manganese addition. Limmer *et al.*^[30] showed that Mn is the only substitutional element to both lower the USFE and the ISFE; thus, making the ε -martensite both easier to form and more stable. Aluminum and silicon both lower the

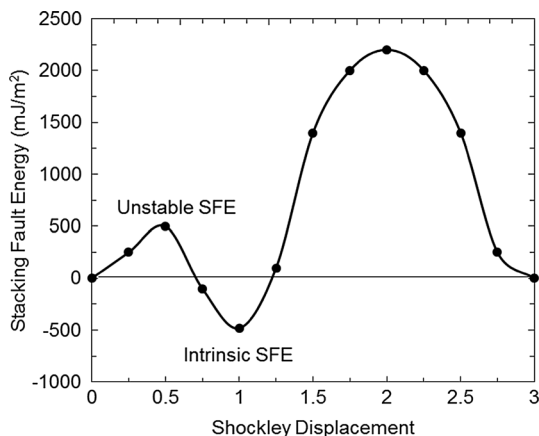


Fig. 1—Generalized stacking fault energy curve for pure Fe calculated by first-principles simulation. Unstable stacking fault energy (USFE) and intrinsic stacking fault energy (ISFE) are shown in the plot at 0.5 and 1.0.

USFE making ε -martensite and dislocation nucleation easier; however, they increase the ISFE.^[29] Medvedeva *et al.*^[29] also calculated that carbon increases the ISFE when placed at the fault plane; however, Mn can help mitigate this increase by forming a Mn-C dipole.

C. Effect of Chemistry

The complex effect of Mn on the martensitic start temperature has been presented in the works of Pisarik and Van Aken^[31] for ε -martensite and Field *et al.*^[32] for α -martensite. Thermodynamic calculations by Pisarik and Van Aken^[31] determined that the ε -martensite start temperature is related to Mn in a parabolic fashion, with a minimum occurring at roughly 12 to 13 wt pct Mn. Similar results were reported by Field *et al.* on the start temperature for α -martensite^[32] and experimental measurements of the α -martensite start temperature yielded two distinct behaviors in the thermodynamic driving force. Alloys that contained greater than 12 wt pct manganese exhibited a greater temperature dependence for the driving force than alloys having less than 12 wt pct and these lower manganese steels exhibited a thermodynamic relation similar to that reported for low-alloy lath martensitic steels. Field *et al.* also showed that both behaviors could be unified to a single equation when the elastic strain energy of transformation was included. However, the proposed model for α -martensite was limited to Mn contents less than 16 wt pct.

It has been reported in literature that alloying with silicon and aluminum affects dynamic and static recrystallization of TRIP steels.^[33–35] Suikkanen *et al.*^[33] found that the rate of static recrystallization linearly decreased with increasing Si up to 1.5 wt pct. This effect has also been observed in the works by Somani *et al.*,^[36] Medina and Mancilla^[37], Medina and Quispe,^[38] and Field and Van Aken.^[21] Hot band properties reported by Field and Van Aken^[21] for medium-Mn steel with 2.4 wt pct Si exhibited a high ultimate tensile strength of 1840 MPa for a partially recovered hot band microstructure making the steel difficult to cold work. Silicon's effect on recrystallization has been rationalized assuming a solute drag effect on grain boundaries. Li-Juan *et al.*^[34] investigated the effect of Si and Mn on the dynamic recrystallization of conventional TRIP steel and showed that Mn had little effect on the dynamic recrystallization; however, they observed that silicon was effective in slowing the dynamic recrystallization and increased the static recrystallization temperature. It was also shown by Zhu *et al.*^[35] that the dynamic recrystallization response is greatly impeded when the silicon content is increased to 1.5 wt pct silicon.

Little has been reported on the influence of Al on the recrystallization of TRIP steel; however, Somani *et al.*^[33] found that Al had a negligible effect on static recrystallization. Aluminum's effect on the properties of first-generation advanced high-strength TRIP steels is considered to be very complicated. Aluminum has been shown to affect the work hardening behavior and the dynamic strain aging (DSA) response of TWIP and TRIP steels.^[19,21,39] It has been shown in the high-Mn TWIP steels that Al additions will reduce the work

hardening rate by reducing the deformation twin density [39]. Lee *et al.* [39] investigated the dynamic strain aging of two TWIP steels, one containing aluminum, 0.6C-18Mn-1.5Al-balFe (wt pct), and the second being an Al-free 0.6C-18Mn-balFe (wt pct) steel, and it was observed that the work hardening rate and ultimate tensile strength were reduced with the addition of aluminum. Lee *et al.* also showed that Al was effective in suppressing the dynamic strain aging of the TWIP steel. Work by Grässel *et al.* [19] shows that the ultimate tensile strength of 15Mn-*x*Si-*y*Al (in wt pct) exhibited a decrease in ultimate tensile strength with increasing aluminum content and that the ductility increased with increasing aluminum content.

Dynamic strain aging (DSA) plays an important role in the work hardening behavior and ductility of medium manganese steels; DSA leads to increased ultimate tensile strengths and reduced ductility as measured by elongation to failure, and the role of nitrogen and carbon has recently been elucidated. Field and Van Aken [21] found that nitrogen in α -ferrite was a potential cause for both static and dynamic strain aging in an intercritically annealed 10 wt pct Mn steel. Two additional DSA mechanisms were identified: trapping of Mn atoms at stacking faults in microstructures containing ε -martensite, and Mn-C defect pairs in γ -austenite.

The purpose of this paper is to elucidate the role of chemistry and ISFE in the microstructural design and processing of medium manganese steels to obtain a two-stage TRIP response. Fundamental to this quest is to better understand how to formulate each Ms temperature and determine if the α -martensite start temperature needs be less than, equal to, or greater than the ε -martensite start temperature to optimize the two-stage TRIP behavior. Although not a primary purpose in this study, the role of silicon and aluminum on recovery, defect retention, and recrystallization of these steels will also be discussed.

II. EXPERIMENTAL PROCEDURE

All of the steels used for this investigation were melted using induction iron, ferrosilicon, electrolytic manganese, pure aluminum, and carbon in the form of graphite. An argon cover gas was used to shield the melt

and calcium wire additions were made to modify oxide inclusions and remove sulfur. Composition was verified by optical emission spectroscopy and adjusted prior to tapping the furnace into a ladle. A modified ladle using a ceramic dam to force liquid from below the surface to form the pouring stream in a manner similar to a teapot was used for pouring the steel. All alloys were cast with 150 K (150 C°) superheat into phenolic no-bake sand molds to form multiple Y-blocks each with dimensions measuring 12.6 × 6 × 1.7 cm. The upper Y-portion of the Y-block acts as a riser, but this was also attached to a Foseco KALPUR insulated riser with a diameter of 13.5 cm and height of 15.3 cm to ensure the soundness of the lower leg of the Y-block casting. The reported chemical analyses were obtained by inductively coupled plasma spectrometry after sample dissolution in hydrochloric and nitric acid. Carbon and nitrogen contents were determined using a LECO CS6000 and a LECO TC500 combustion analyzers. Alloy composition, calculated room temperature ISFE, and martensite start temperatures are listed in Table I. The martensite start temperatures were calculated according to the works of References 31 and 32. For brevity, alloys will be designated by the room temperature (298K, 25 °C) calculated ISFE values (bulk composition) and designated in the form # SFE. Stacking fault energies were calculated using Olson and Cohen's equation [41] shown below as Eq. [2].

$$\text{SFE}(\text{mJ}/\text{m}^2) = n\rho(\Delta G^{\gamma \rightarrow \varepsilon}) + 2\sigma^{\gamma/\varepsilon}. \quad [2]$$

The driving force for transformation, $\Delta G^{\gamma \rightarrow \varepsilon}$, was obtained using an updated regular solution model, [31] $n = 2$, ρ is the planar atomic density of the $\{111\}_\gamma$ and calculated using alloy chemistry and Vegard's law, and $\sigma^{\gamma/\varepsilon}$ is the interfacial energy between the γ -austenite and ε -martensite, which was held constant at 10 mJ/m² according to the results of Pisarik and Van Aken. [31]

A start temperature for the ε -martensite was calculated by determining the temperature at which SFE = 0 mJ/m² for the case where $n = 4$. [31] The α -martensite start temperature, M_s^α , was calculated according to the work by Field and Van Aken, [32] where the strain energy of transformation, ($\Delta G_{\text{str}}^{\gamma \rightarrow \alpha}$) was balanced against the chemical driving force ($\Delta G_{\text{Chem}}^{\gamma \rightarrow \alpha}$) according to Eq. [3] and Eq. [4].

Table I. Austenite Composition and the Calculated Start Temperature for the ε and α Martensites

Alloy	Composition (Weight Percent)					Calculated Parameters	
	Mn	Si	Al	C	N	Ms ^ε in K (°C)	Ms ^α in K (°C)
13.3 SFE	13.9	2.07	2.01	0.09	0.012	284 (11)	397 (124)
13.0 SFE	11.1	1.37	1.49	0.27	0.018	274 (1)	371 (98)
7.8 SFE	15.1	1.95	1.40	0.08	0.017	311 (38)	424 (151)
5.0 SFE	14.3	2.97	0.89	0.16	0.022	360 (87)	428 (155)
– 0.2 SFE	10.2	2.38	0.30	0.17	0.024	387 (114)	417 (144)
– 1.8 SFE	11.5	2.46	0.38	0.11	0.029	400 (127)	383 (110)
– 2.1 SFE	13.8	2.01	0.40	0.10	0.028	405 (132)	381 (108)
– 2.2 SFE	13.0	1.57	0.45	0.10	0.045	404 (131)	354 (81)

$$\Delta G_{\text{Chem}}^{\gamma \rightarrow \alpha} + \Delta G_{\text{Str}}^{\gamma \rightarrow \alpha} = 0 \quad [3]$$

$$\Delta G_{\text{Str}}^{\gamma \rightarrow \alpha} (\text{J/mol}) = E\Omega\delta^2(14.8 - 0.013T), \quad [4]$$

where $\Delta G_{\text{Chem}}^{\gamma \rightarrow \alpha}$ is calculated according to a modified regular solution model described in Field *et al.*,^[32] Ω is the molar volume for iron of 7.15×10^{-6} (m³/mol), δ is the lattice misfit between the γ -austenite and α -martensite with an approximate strain of 1.11×10^{-2} (m/m), T is the temperature in Kelvin, and E is the modulus in units of Pa. The start temperature for the α -martensite was calculated by determining the temperature where Eq. [3] is true.

Steel castings were normalized at 1373 K (1100 °C), held at temperature for 2 hours, and air cooled to 298 K (25 °C). Normalized castings were milled to an orthogonal prism of dimensions $15.5 \times 125 \times 50$ mm³ and hot rolled sequentially by heating to 1223 K (950 °C), rolling, and reheating to 1223 K (950 °C). This was repeated to obtain a hot band gage of 2.5 mm. A total hot reduction of 87.2 ± 6.8 pct was accomplished and an exit temperature of 1068 ± 15 K (775 °C) was measured after the final roll pass to obtain the desired hot band thickness. Hot band tensile properties were measured to determine a target range for cold rolling. Experience processing these alloys suggested that the cold rolling reduction be limited to a range of two to three times the total elongation measured for the hot band condition. Alloys were cold rolled using a Stanat TA 315 in a 4-high roll configuration. Industrial batch annealing was mimicked by placing the cold rolled sheet into stainless steel bags and heated to 873 K (600 °C) at a rate of 20 K/min, allowed to equilibrate at temperature, holding for 20 hours, and air cooled to 298 K (25 °C) at an average rate of 10 K/min. Gray iron machining chips were added to the stainless steel bags to provide atmosphere protection.

Tensile bars were cut from both the hot band and batch-annealed materials parallel to the rolling direction and the gage edge was milled to produce a standard ASTM E8^[42] tensile bar with a gage length of 50 mm and gage width of 12.5 mm. Gage width surfaces were not ground or machined. Tensile tests were conducted at room temperature and Young's modulus was determined using a clip-on extensometer. Tests were performed in displacement control at a rate of 0.01 mm/sec using a 245 kN servo-hydraulic test frame. A non-contact laser extensometer was used to measure the total strain to failure.

X-ray diffraction (XRD) patterns were collected for all mechanically tested conditions to investigate the microstructural development during processing. XRD samples were mechanically polished to 0.1 μ m using diamond paste in the Longitudinal-Transverse plane, (polished surface parallel to the rolling plane) and diffraction patterns were obtained with a Phillips X-pert diffractometer using Cu K α radiation with a nickel filter and a flat graphite monochromator. Phase quantifications were calculated utilizing the Rietveld refinement described by Martin *et al.*^[43] on an Fe-16Cr-6.8Mn-6.1Ni steel for ε -martensite analysis

and modified for the steel chemistry being investigated in this study. Work to correlate the total volume change from the various phases present and total tensile elongation was done on the alloys in both the hot band and batch-annealed steels. The lattice parameters of the γ -austenite, ε -martensite, and α -martensite crystalline phases were measured using transmission electron microscopy. A percent change in volume was calculated according to Eq. [5].

$$\Delta V^{i \rightarrow f} (\text{pct}) = 100 \text{ pct} \left(\frac{V^i - V^f}{V^i} \right) \quad [5]$$

V^i is the volume of the initial phase and V^f is the volume of the final phase, the total volume change is then calculated by Eq. [6].

$$\Delta V_{\text{total}} = \Delta V^{\gamma \rightarrow \varepsilon} (\gamma_{\text{volpct}}) + \Delta V^{\varepsilon \rightarrow \alpha'} (\gamma_{\text{volpct}} + \varepsilon_{\text{volpct}}) \quad [6]$$

Specimens for electron back-scattered diffraction (EBSD) were mechanically polished with a 0.02 μ m colloidal silica solution using a vibratory polisher and examined in the Longitudinal-Short plane (perpendicular to both the rolling plane normal and the rolling direction). Orientation image mapping *via* pattern analysis was performed on a Helios Nanolab 600 using a Nordlys detector and the Aztec 3.3 software package. The electron beam was operated at an accelerating voltage of 20.0 kV and an emission current 11 nA. Electron dispersive spectroscopy (EDS) mapping was conducted simultaneously to the EBSD mapping using a lithium-drifted silicon detector with the same parameters for EBSD mapping. Orientation image maps and diffraction patterns were tilt corrected for the system geometry. Degree of recrystallization was determined using the post-processing software Channel 5 on multiple EBSD maps to produce a total measured area of 0.1 mm², grains containing internal misorientation greater than 5 deg were considered deformed, and grains with misorientation less than 1 deg were considered recovered. Grain size was measured according to the ASTM E112—13 using the Heyn Lineal Intercept method. Transmission electron microscopy (TEM) analysis was performed using an FEI Tecnai F20 TEM. Thin foils for TEM analysis were analyzed in the Longitudinal-Transverse plane and prepared using a solution of 6 pct perchloric acid, 60 pct methanol, and 34 pct butoxyethanol, and a dual-jet electropolishing system operating at 243 K (− 30 °C) utilizing a DC current of 10 to 12 mA to keep a constant voltage of 20 V. The electron beam was operated at an accelerating voltage of 200 kV.

III. RESULTS

Stress–strain plots of the hot band and annealed condition are shown in Figure 2. A summary of the tensile properties is listed in Table II. Microstructural characterizations as performed by XRD to determine phase percentages are shown in Table III. Only alloys

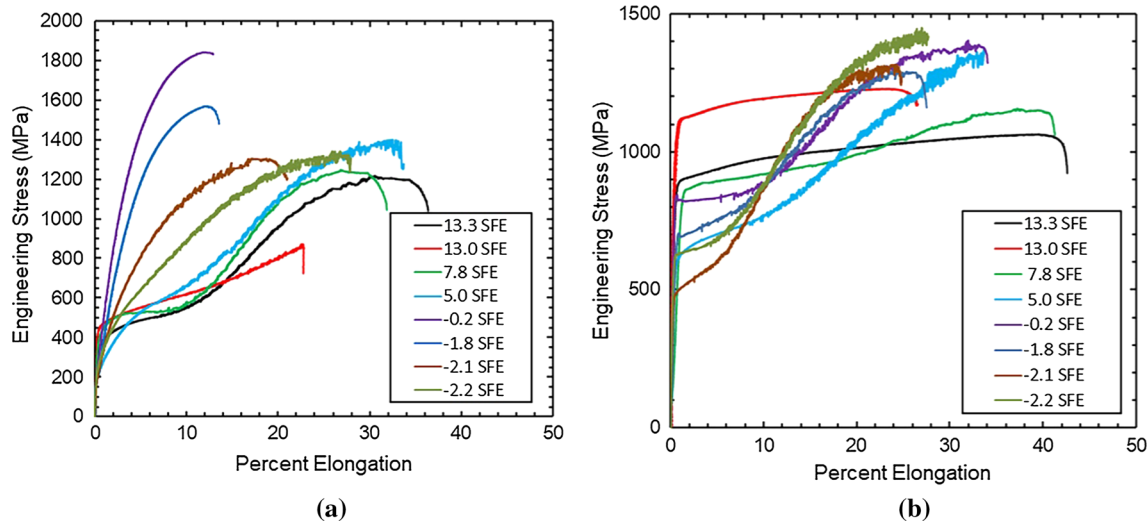


Fig. 2—Stress–strain graph of the (a) hot band and (b) cold worked and annealed steels (Color figure online).

Table II. Mechanical Properties and Measured Mean Free Microstructural Path (L_3) of the Hot Band and Processed Steel

Alloy	Hot Band				Cold Work (Percent)	Cold Worked and Annealed			
	YS (MPa)	UTS (MPa)	e_f (Percent)	L_3 (μm)		YS (MPa)	UTS (MPa)	e_f (Percent)	L_3 (μm)
13.3 SFE	330	1220	36.4	11.7	65.1	880	1060	42.6	0.48
13.0 SFE	450	785	19.1	12.2	55.0	1120	1330	26.5	0.68
7.8 SFE	380	1250	31.9	13.9	66.4	850	1160	41.3	0.35
5.0 SFE	205	1400	33.7	23.0	69.3	595	1370	33.7	1.56
– 0.2 SFE	260	1840	12.9	16.2	35.6	840	1400	34.1	0.34
– 1.8 SFE	210	1570	13.6	17.2	33.2	790	1300	27.5	0.50
– 2.1 SFE	240	1300	21.0	10.7	53.6	500	1320	24.8	1.31
– 2.2 SFE	255	1340	28.0	10.6	57.1	615	1450	27.7	1.23

with positive stacking fault energies exhibit two different and sequential stages, or rates, of work hardening in the hot band materials: an initial stage with a low work hardening rate typically associated with ε -martensite formation and a subsequent rapid work hardening rate during the formation of α -martensite as shown in Figure 2(a). The observation of two different rates of work hardening is often described as an inflection in the stress–strain curve but should not be confused with a yield point elongation phenomenon. Hot band steels containing more than 30 pct γ -austenite (and SFE > 0) produce a yield strength less than 380 MPa, a low work hardening rate ($n \sim 0.05$), and elongations on the order of 3 to 7 pct prior to the onset of rapid work hardening. After cold working and annealing, alloys with a bulk ISFE < 13 mJ/m² exhibit an inflection in the stress vs strain plot as shown in Figure 2(b). From Table III, it is also noted that the alloys with a bulk ISFE ≥ 7.8 mJ/m² do not contain any ε -martensite in the starting microstructure. To determine if these alloys exhibited the two-stage TRIP phenomenon, XRD was performed on partially strained sections of the tensile bar and these results are shown in Figure 3 for the 7.8, 13.0, and 13.3

SFE alloys. The 7.8 SFE alloy does exhibit ε -martensite formation from strains as low as 5 pct, whereas XRD patterns of the 13.0 SFE and 13.3 SFE alloys do not contain ε -martensite in either the partially strained or the region of final failure. From this result, it can be deduced that the 13.0 and 13.3 SFE alloys are not two-stage TRIP alloys.

A Q-R factorization to obtain a least squares fit was used to determine an empirical relationship between the chemistry and ultimate tensile strength and total elongation for the batch-annealed steels exhibiting two-stage TRIP behavior, *i.e.*, alloys with bulk ISFE less than 13 mJ/m². The derived relationships are shown in Eqs. [7, 8] where x_i represents weight percent alloying element “*i*,” it should be noted that carbon and nitrogen have large positive effect upon the ultimate strength. A comparison of the calculated and measured strength is shown in Figure 4 and a relative error of ± 0.05 pct was determined for the tested materials.

$$\begin{aligned}
 UTS(\text{MPa}) = & 2579(x_c) + 13.3(x_{Mn}) - 41.7(x_{Si}) \\
 & - 29.4(x_{Al}) + 72.4(x_{Cr}) + 7818(x_N) \\
 & + 747
 \end{aligned}
 \quad [7]$$

Table III. Phase Quantities of the Hot Band and Processed Steel Measured Using X-ray Diffraction

Alloy	Hot Band			Cold Worked and Annealed		
	γ -austenite (Volume Percent)	ε -martensite (Volume Percent)	α -martensite (Volume Percent)	γ -austenite (Volume Percent)	ε -martensite (Volume Percent)	α -ferrite/ martensite (Volume Percent)
13.3 SFE	95	0	5	64	0	31
13.0 SFE	94	0	6	81	0	19
7.8 SFE	79	0	21	60	0	40
5.0 SFE	93	7	0	64	30	6
– 0.2 SFE	20	26	54	32	10	58
– 1.8 SFE	24	24	52	34	13	53
– 2.1 SFE	14	45	41	67	14	19
– 2.2 SFE	36	21	43	64	33	3

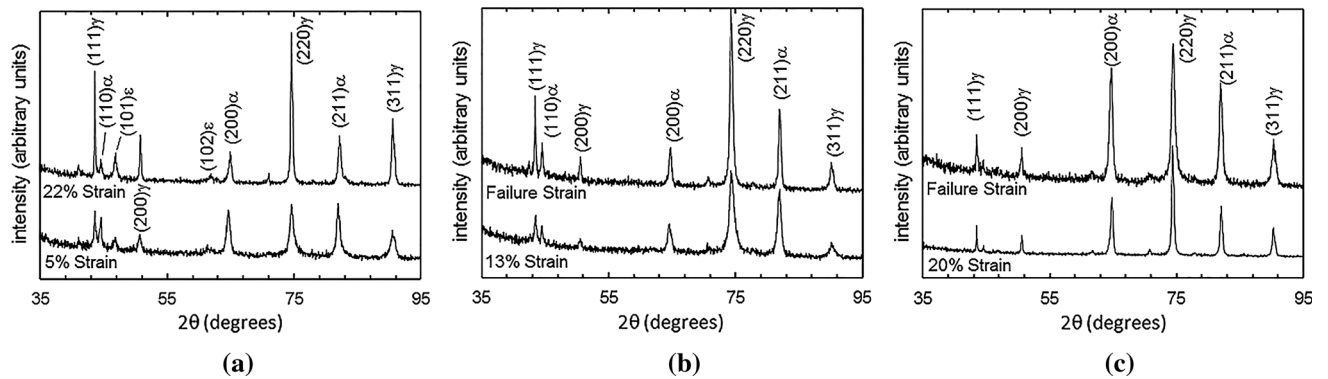


Fig. 3—X-ray diffraction of the partially strained (a) 7.8 SFE, (b) 13.0 SFE, and (c) 13.3 SFE alloys, with the peak positions labeled for the γ -austenite, α -ferrite/martensite, and ε -martensite.

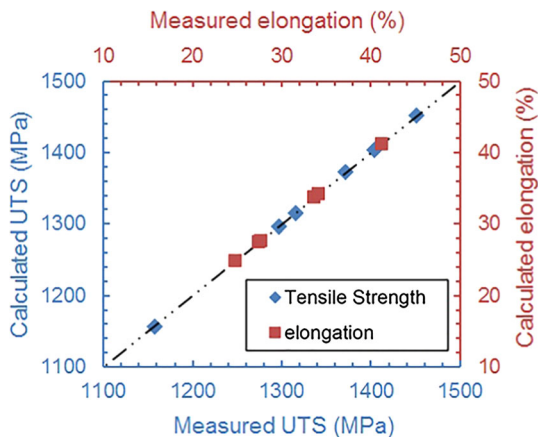


Fig. 4—Graphical comparison of the calculated properties to the measured values showing a fit of ± 0.05 pct with alloys exhibiting two-stage TRIP behavior, ($ISFE < 10 \text{ mJ/m}^2$).

$$Pct\epsilon_{tot} = 77(x_c) - 2.0(x_{Mn}) - 5.0(x_{Si}) + 19.1(x_{Al}) + 5.8(x_{Cr}) - 115(x_N) + 50.6 \quad [8]$$

EBSD phase maps were utilized to quantitatively determine the grain size or mean free path in multiphase microstructures and phase constitution of the hot band and batch-annealed alloys. EBSD phase maps showing grain size are shown in Figure 5(a) for the – 2.2 SFE and Figure 5(b) for the 13.3 SFE steels in the hot band condition. The cold worked and annealed steels exhibit a high degree of microstructural refinement as shown in Figure 6 for the eight alloys tested. Two types of microstructures were developed after batch annealing. The 13.3, 13.0, 7.8, – 0.2, and – 1.8 SFE alloys produced microstructures consistent with an intercritical anneal to obtain an $\gamma + \alpha$ -ferrite dual-phase microstructure and these steels exhibit the highest degree of microstructural refinement. The 5.0, – 2.1, and – 2.2 SFE alloys exhibited a larger grained ($> 2 \mu\text{m}$) γ -austenite with athermal martensites ($\varepsilon + \alpha$); for these three alloys, the batch annealing temperature of 873 K (600 °C) produced a nearly 100 vol pct γ -austenite microstructure. The average mean free path (L_3) between phase boundaries measured in the batch-annealed (cold worked and annealed) steel ranged from 320 nm to 1.3 μm .

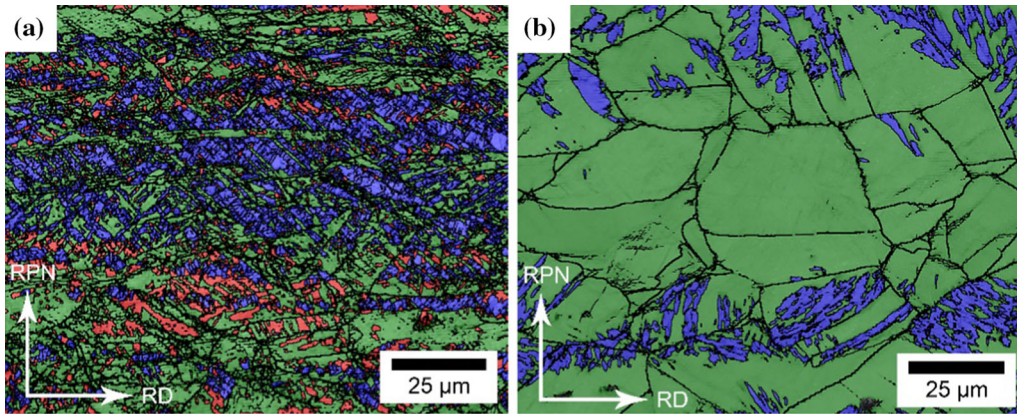


Fig. 5—EBSD phase map of the hot band (a) – 2.2 SFE (Si/Al = 3.49) where prior γ -austenite grain boundaries are darkened and (b) 13.3 SFE (Si:Al = 1.03) steels. γ -austenite is green, ϵ -martensite is red, and α -martensite is blue (Color figure online).

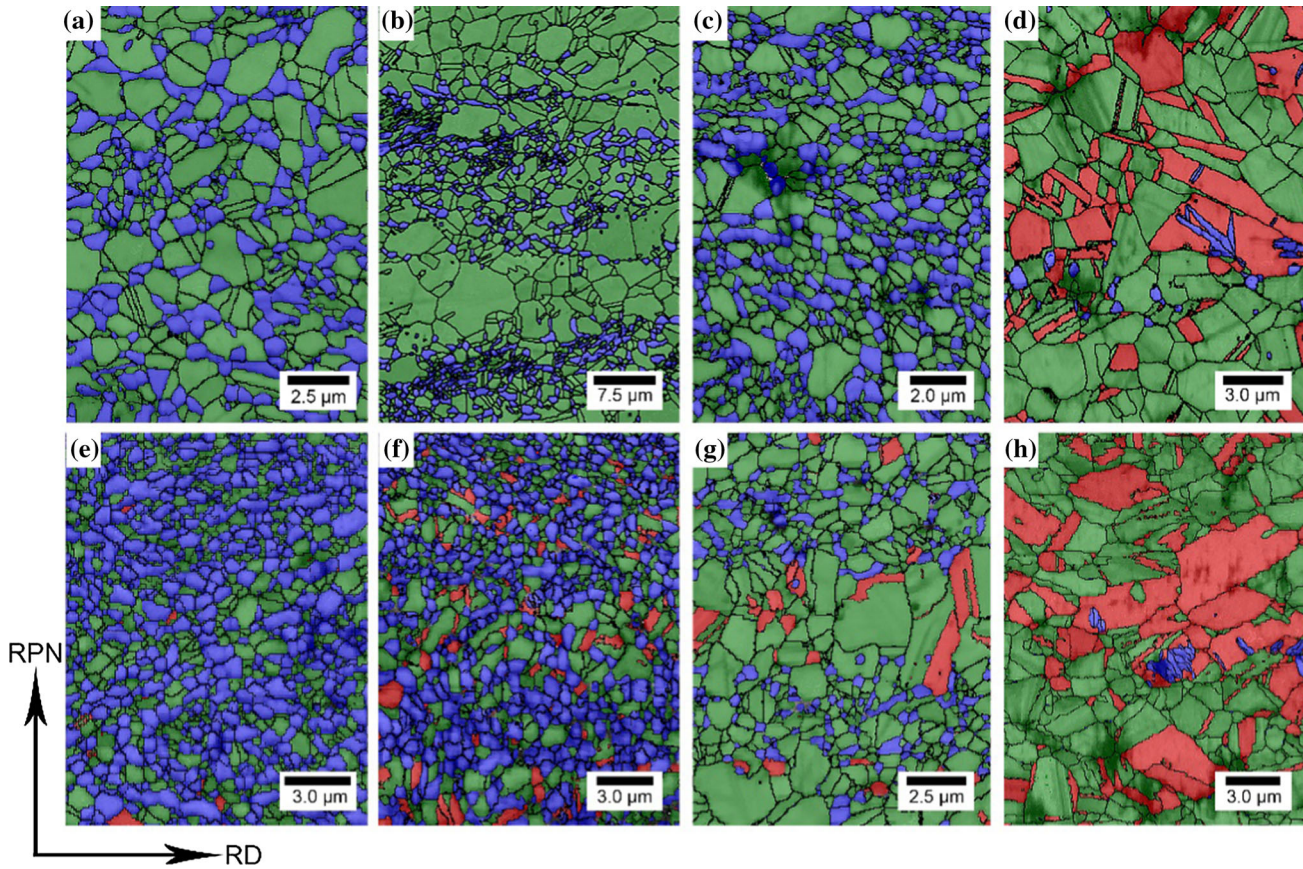


Fig. 6—EBSD phase map of the cold worked and annealed steel (a) 13.3 SFE, (b) 13.3 SFE, (c) 7.8 SFE, (d) 5.0 SFE, (e) – 0.2 SFE, (f) – 1.8 SFE, (g) – 2.1 SFE, and (h) – 2.2 SFE alloys. γ -austenite is green, ϵ -martensite is red, and α -ferrite is blue (Color figure online).

A Hall–Petch grain size (or mean free path) dependence for yield strength is graphed in Figure 7 for the eight alloys tested and 43 additional alloys from literature^[6,8,11,39,46–57] with grain diameters ranging from 30 to 0.30 μm . Data were taken from austenitic stainless steel, dual-phase α -martensite/ α -ferrite, and medium-Mn steels. A linear fit is shown for the data presented in this study, but the 13.0 SFE alloy was

excluded because the grain size was bimodal. Figure 7(b) compares the mean free path to yield strength relationship for the alloys presented in this study and previously reported medium-Mn steels. The Hall–Petch grain size relationship shown in Figure 7 is very similar to that reported by Lee *et al.*^[13] as shown in Eq. [1] with a similar grain boundary hardening term, K , (388 $\text{MPa } \mu\text{m}^{1/2}$ vs 332 $\text{MPa } \mu\text{m}^{1/2}$) and friction stress,

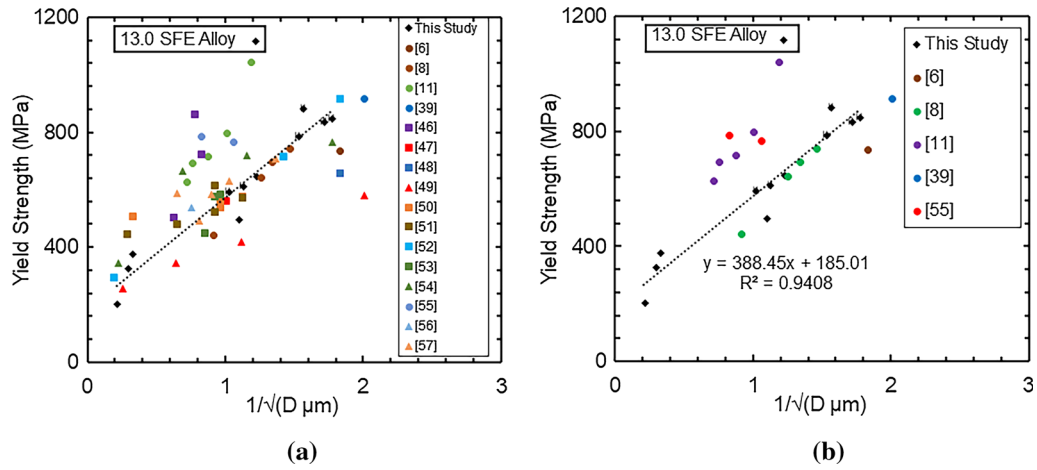


Fig. 7—(a) Comparison of the Hall–Petch inverse root grain size (or mean free path) relationship of alloys produced in this study to reported austenitic stainless steels (triangles), dual-phase steels (squares), and medium-Mn steels (circles). (b) Hall–Petch relationship for medium-Mn steels and the steels presented in this work. The line fit is restricted to measurements of this study and is the same in both graphs. The 13.0 SFE alloy was excluded due to the highly bimodal grain size (Color figure online).

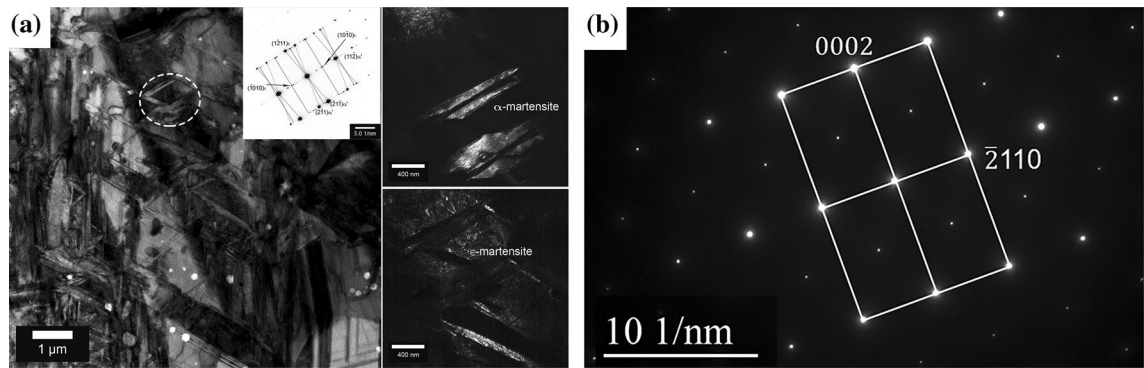


Fig. 8—(a) Transmission electron micrograph of the -2.2 SFE alloy showing the two-stage TRIP products of ϵ -martensite and α -martensite and the selected area diffraction pattern (inset) utilized for dark-field imaging of the ϵ -martensite and α -martensite. The beam direction is parallel to the $[\bar{1}2\bar{1}6]$ zone axis of ϵ -martensite and $[153]$ zone axis of α -martensite. (b) Selected area diffraction of the $[0\bar{1}10]$ zone axis of the ϵ -martensite.

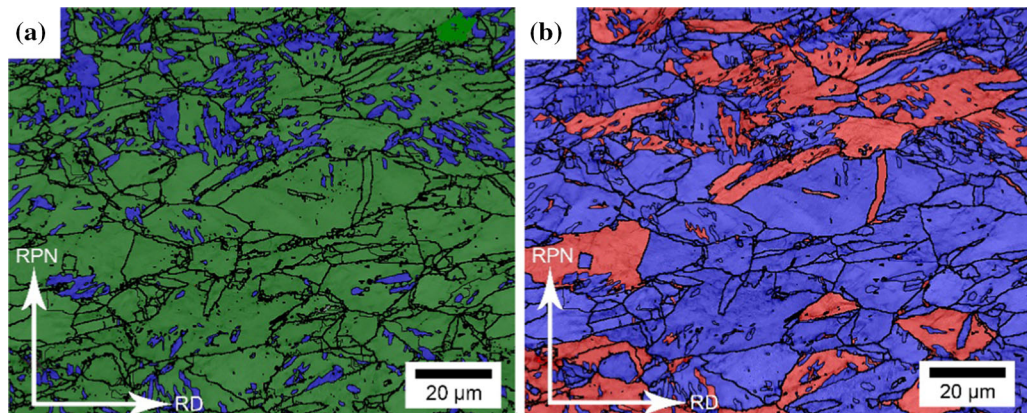


Fig. 9—(a) Phase map of the 7.8 SFE alloy in the hot band condition where green is γ -austenite and blue α -ferrite/martensite. (b) Recrystallization map of the 7.8 SFE alloy where blue grains are defined as recrystallized and red grains are defined as substructured and deformed grains. The Si:Al of this alloy is 1.39 (Color figure online).

σ_0 , (185 MPa vs 223 MPa) and is discussed in greater detail below.

Transmission electron microscopy (TEM) was utilized to better determine the lattice parameters of the three phases of interest γ , ε , and α . A TEM micrograph is shown for the -2.2 SFE steel in Figure 8 with the associated diffraction patterns. TEM was utilized to confirm the ε -martensite phase and determine the lattice parameters: $a = 2.62 \text{ \AA}$, $c = 4.09 \text{ \AA}$, and $c/a = 1.56$. The lattice parameters for α -martensite were $a = 2.88 \text{ \AA}$, $c = 2.91 \text{ \AA}$. The austenite lattice parameter was measured to be 3.68 \AA . A Shoji–Nishiyama orientation relationship was observed between the parent γ -austenite and the ε -martensite and is in agreement with previous work on the γ , ε , and α orientation relationships observed for athermal^[45] and strain-induced^[24] martensites.

From the EBSD-OIM mapping, the degree of recovery/recrystallization was measured for the hot band condition to examine the role of Si and Al on the tensile behavior of these steels. The degree of recovery/recrystallization was measured from multiple maps on each specimen to obtain a total map size of $0.1 \pm 0.02 \text{ mm}^2$.

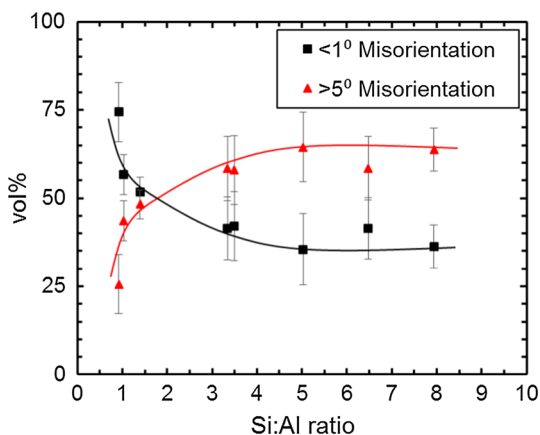


Fig. 10—The state of deformation measured according to EBSD-OIM, volume fraction of both the recrystallized and deformed grains are determined by the mean angular distribution as a function of silicon-to-aluminum ratio.

A representative phase map and recovery/recrystallization OIM map of the 7.8 SFE steel are shown in Figure 9, and it is observed that there are twinned γ -austenite grains in the structure; however, many of the annealing twins appear bent and the grain aspect ratio shows an elongation parallel to the rolling plane. The vol pct recovered/recrystallized, defined as less than 1 deg of misorientation within the grain, and deformed, defined as greater than 5 deg of misorientation within the grain, relative to the Si/Al ratio is shown in Figure 10 with the uncertainty measured to a 95 pct confidence level. In general, a non-linear behavior is found showing that a greater resistance to recovery/recrystallization is observed with increasing Si/Al ratio.

Partitioning of the alloying elements during intercritical annealing at 873 K (600 °C) heat treatment occurs and can be used to differentiate α -ferrite formed during the 873 K (600 °C) anneal and athermal α -martensite. Figure 11 shows both phase mapping and alloy partitioning of Al and Mn for the 13.3 SFE and 5.0 SFE alloys. Both equiaxed α grains and lenticular α -martensite within ε -martensite bands are shown in blue. Energy-dispersive X-ray spectroscopy (EDS) mapping reveals that equiaxed α -ferrite grains formed during annealing are rich in aluminum and lean in Mn, whereas the lenticular α -martensite within the ε -martensite bands, shown by arrows in Figure 11(b), could not be differentiated from the γ -austenite by composition. In general, α -martensite was observed within the ε -martensite bands as previously reported by De Cooman *et al.*^[20] and Field and Van Aken.^[21] A summary of the compositions measured from EDS analysis is shown in Table IV. Equilibrium calculations performed using FactSage 7.0 with the FSstel database are also included in Table IV for reference. To better replicate the composition of the α -ferrite and γ -austenite composition using the thermodynamic software, a temperature was determined to reproduce the measured α -ferrite volume fraction from Table III and adjustments were made from the EBSD analysis if only α -martensite was observed as was the case with the -2.2 SFE steel. It was also assumed that the total γ -austenite at the batch annealing temperature included athermal ε -martensite.

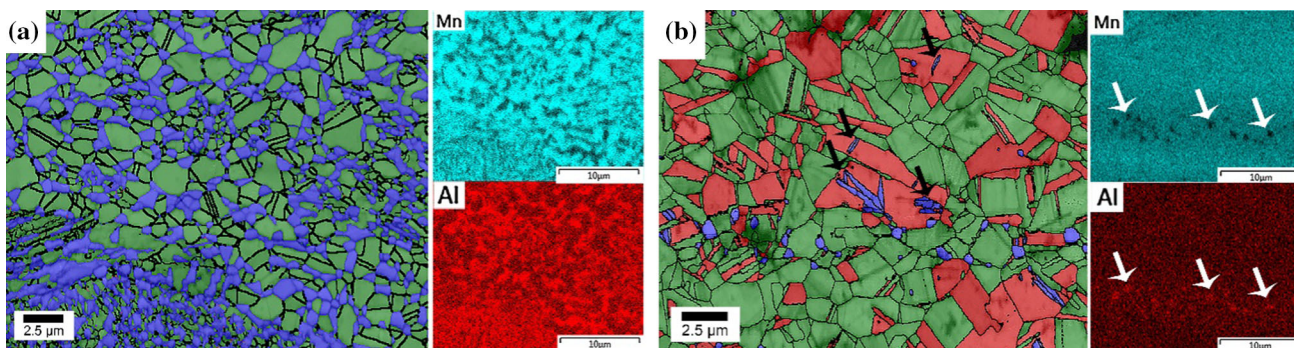


Fig. 11—(a) An EBSD phase map and the distribution of Mn and Al, in 13.3 SFE alloy and (b) EBSD phase map and the distribution of Mn and Al in the 5.0 SFE alloy where α -martensite is highlighted by black arrows in the EBSD phase map and the α -ferrite is highlighted by white arrows in the EDS maps. α -ferrite/ α -martensite (blue) grains show increased concentration of aluminum and reduced concentration of manganese, and conversely for the γ -austenite (green) (Color figure online).

Table IV. Measured Composition of the γ -Austenite and α -Ferrite After Cold Working and Annealing the Steels at 873 K (600 °C) with a 95 pct Confidence Level Standard Deviation. Thermodynamic Calculations of the Phase Composition Performed to Match Measured Phase Quantities. M_s^x was not Calculated for γ -Austenite Compositions Greater than 14 Weight Percent Mn due to the Model Limitation Described in the Work by Field *et al.*^[32]

Phase	EDS										FactSage								
	(Composition Weight Percent)										Temperature			(Composition Weight Percent)					
	Mn	Si	Al	C*	N*	SFE (mj/m ²)	Ms ^γ K	Ms ^α K	Ms ^γ K	Ms ^α K	FactSage Temperature K (°C)	Mn	Si	Al	C	N	Ms ^γ K	Ms ^α K	
13.3SFE	γ	18.0 ± 0.8	1.95 ± 0.34	1.45 ± 0.29	0.12	0.03	12.1	279	—	813 (540)	18.5	2.10	1.76	0.13	0.021	243	—		
α	12.5 ± 1.0	2.06 ± 0.23	2.32 ± 0.27	0.02	0.10	—	—	—	—	—	4.06	2.00	2.57	< 0.001	0.008	—	—		
13.0SFE	γ	12.4 ± 2.2	1.41 ± 1.1	1.25 ± 0.55	0.33	0.01	11.9	283	431	793 (520)	13.1	1.41	1.38	0.37	0.022	267	465		
α	10.4 ± 1.2	1.51 ± 0.22	1.43 ± 1.0	0.02	0.10	—	—	—	—	—	2.92	1.21	1.96	< 0.001	0.002	—	—		
7.8SFE	γ	16.8 ± 1.0	1.68 ± 0.21	1.42 ± 0.21	0.12	0.04	10.5	259	—	818 (545)	21.0	1.96	1.16	0.12	0.033	258	—		
α	12.5 ± 2.8	1.73 ± 0.23	1.90 ± 0.39	0.02	0.10	—	—	—	—	—	4.25	1.94	1.76	< 0.001	0.007	—	—		
5.0SFE	γ	16.3 ± 1.5	2.47 ± 0.42	0.72 ± 0.11	0.17	0.02	4.7	340	—	803 (530)	15.1	2.92	0.79	0.19	0.025	329	—		
α	11.7 ± 2.6	2.6 ± 1.22	1.03 ± 0.23	0.02	0.10	—	—	—	—	—	4.52	3.16	1.99	< 0.001	0.005	—	—		
- 0.2SFE	γ	12.3 ± 3.0	2.1 ± 0.52	0.23 ± 0.11	0.36	0.08	3.3	340	421	793 (520)	18.4	2.14	0.19	0.40	0.056	323	—		
α	9.01 ± 3.3	2.5 ± 1.32	0.32 ± 0.21	0.02	0.10	—	—	—	—	—	4.22	2.55	0.38	< 0.001	0.011	—	—		
- 1.8SFE	γ	13.1 ± 0.8	1.63 ± 0.23	0.26 ± 0.14	0.21	0.05	- 0.9	374	396	788 (515)	18.5	2.31	0.23	0.22	0.043	350	—		
α	10.2 ± 1.7	1.75 ± 0.23	0.39 ± 0.13	0.02	0.10	—	—	—	—	—	4.62	2.62	0.51	< 0.001	0.017	—	—		
- 2.1SFE	γ	15.9 ± 3.1	1.97 ± 0.41	0.38 ± 0.12	0.11	0.01	- 0.7	376	—	833 (560)	16.0	2.00	0.27	0.14	0.051	371	—		
α	10.9 ± 2.1	2.21 ± 1.10	0.41 ± 0.11	0.02	0.10	—	—	—	—	—	4.03	1.99	0.87	< 0.001	0.070	—	—		
- 2.2SFE	γ	13.1 ± 1.4	1.48 ± 0.21	0.43 ± 0.29	0.10	0.04	- 2.2	384	357	—	—	—	—	—	—	—	—		
α	—	—	—	—	—	—	—	—	—	—	—	—	—	—	—	—	—		

*Values determined assuming full partitioning to the γ -austenite in the absence of AlN

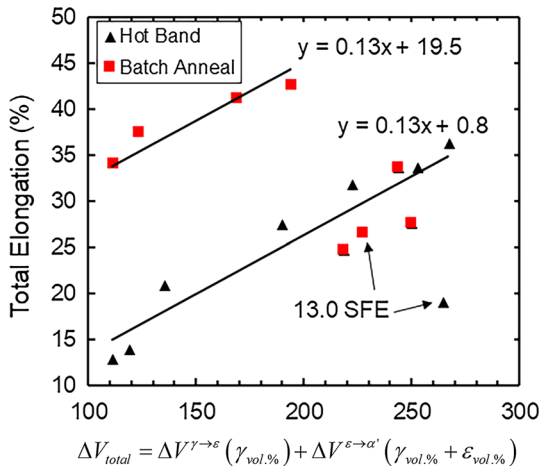


Fig. 12—Volume percent transformable product multiplied by the volume change associated with its martensitic reaction and its effect on the total elongation for the steels exhibiting the two-stage TRIP steels (ISFE ≤ 7.8 mJ/m²).

Carbon and nitrogen reported in Table IV are calculated assuming full partitioning to the γ -austenite and the absence of AlN. The average calculated temperature that matched the measured α -ferrite was found to be 808 ± 17 K (535 °C). The 65 K (65 °C) difference in temperature between calculated and experimental annealing temperature to match the α -ferrite content is likely due to (1) the alloy systems being non-dilute and (2) the kinetics for substitutional diffusion are sluggish at the intercritical annealing temperature and paraequilibrium partitioning might not have been obtained in the 20-hour treatment.

Total elongation to failure was correlated to the lattice parameter and the calculated volume change associated with the two martensitic reactions determined according to Eqs. [5] and [6] and is shown in Figure 12. It should be noted that there is a volume contraction associated with the $\gamma \rightarrow \varepsilon$ martensitic transformation and this leads to a negative contribution to the total volume change. Two parallel trends are observed. Alloys that contain equiaxed α -ferrite after batch annealing have a greater total ductility for an equivalent volume change compared to the hot band alloys. Batch-annealed alloys that are coarser grained ($> 2 \mu\text{m}$) contain α primarily in the form of α -martensite and exhibit behavior similar to the hot band alloys with respect to total elongation to failure.

IV. DISCUSSION

A summary of the property data is shown in Figure 13 relative to the goals set by the U.S. Department of Energy for 3rd generation advanced high-strength steel. In terms of ultimate tensile strength and total elongation to failure many of the alloys studied here demonstrate the requisite properties in either the hot band or batch-annealed condition. Two of the hot band steels (-0.2 SFE and -1.8 SFE) have properties equivalent to press hardened martensitic steels with

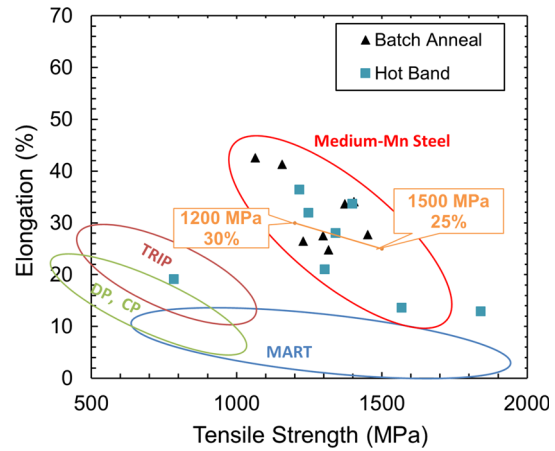


Fig. 13—Population plot of the reported medium manganese steels. DOE targets are shown for 3rd generation advanced high-strength steels with designed medium-Mn steels outlined within the oval.

ultimate strengths as high as 1840 MPa and total elongation to failure of 12.9 pct. It should be noted with emphasis that a simple process of hot working and air-cooling obtained these properties. Both the -0.2 SFE and -1.8 SFE steels have the highest Si:Al ratio for the chemistries studied and produced a partially recrystallized microstructure in the hot band condition (see Figure 10). The microstructure for these two steels contained mostly (> 50 vol pct) α -martensite and equal proportions of ε -martensite and γ -austenite (see Table III). It is reasonable to assume that the mechanical behavior of the hot band steels is dependent upon the ease of recrystallization coming off of the roll mill. As previously noted in literature, silicon^[33–35] is thought to reduce grain boundary mobility during recrystallization; however, as shown in Figure 10 the addition of Al appears to mitigate this drag effect when present in equal or greater proportion, *i.e.*, Si:Al ≤ 1.0 .

Tensile strength and total ductility of the cold worked and annealed alloys were empirically related to the chemistry in Eqs. [7, 8]. The 13.3 and 13.0 SFE alloys were excluded from the model because they were observed to exhibit a TWIP–TRIP response. From the results of Eqs. [7] and [8], it is noted that both carbon and nitrogen have large positive effects on the tensile strength of these two-stage TRIP alloys. Nitrogen also appears to have a negative effect on the total ductility and this dual effect is potentially tied to the DSA response observed in these steels.^[21] A summary of the strain aging response of the steels investigated is shown in Table V with the concentration of Mn, C, and Al in the annealed γ -austenite according to the EDS results. The concentration of carbon assuming complete partitioning to γ -austenite, the calculated concentration of nitrogen in α -ferrite using FactSage, and the total α -ferrite measured using EBSD phase maps are listed in Table V. Alloys with > 50 vol pct α -ferrite (-0.2 SFE and -1.8 SFE) exhibit both DSA and yield point behavior which according to the work by Field and Van Aken^[21] is due to nitrogen pinning of dislocations in α -ferrite. Table V also identifies these alloys as having

Table V. Dynamic Strain Aging and Yield Point Observation with Respect to Alloy Concentration in the α -Ferrite and γ -Austenite. Volume Fraction of α -Ferrite Measured After Intercritical Annealing Using EBSD Phase Maps

Alloy	DSA	Yield Point	Concentration in γ -austenite (Weight Percent)			Concentration in α -ferrite (Weight Percent)		
			Al	Mn	C*	α -ferrite (V_f)	C*	N [#]
13.3 SFE	None	None	1.45	18.0	0.12	0.31	< 0.001	0.008
13.0 SFE	None	None	1.25	12.4	0.33	0.19	< 0.001	0.002
7.8 SFE	Late Stage	None	1.42	16.8	0.12	0.40	< 0.001	0.007
5.0 SFE	Strong DSA	None	0.72	16.3	0.17	0.03	< 0.001	0.005
– 0.2 SFE	Strong DSA	Yes	0.23	12.3	0.36	0.58	< 0.001	0.011
– 1.8 SFE	Strong DSA	Yes	0.26	13.1	0.21	0.53	< 0.001	0.017
– 2.1 SFE	Strong DSA	None	0.38	15.9	0.11	0.08	< 0.001	0.007
– 2.2 SFE	Strong DSA	None	0.43	13.1	0.10	0.00	—	—

*Values calculated assuming full partitioning to the γ -austenite.

#Values calculated using FactSage 7.0 using the FSstel database.

the highest concentration of N (> 0.011 wt pct) in the α -ferrite and is consistent with previously reported results.^[21]

Results from this study also corroborate the DSA mechanism associated with Mn trapping at stacking faults or ε -martensite/ γ -austenite interfaces reported previously.^[21] Alloys with significant ε -martensite content in the starting microstructure (ISFE < 5.0 mJ/m²) show significant DSA upon yielding as shown in Figure 2(b). It is interesting to note that alloy 7.8 SFE does not contain ε -martensite in the starting microstructure (see Table III) and does not exhibit significant DSA until plastic strains of 10 pct or greater. At 5 pct plastic strain, the amount of ε -martensite in the alloy 7.8 SFE was measured to be 23 vol pct by X-ray diffraction as shown in Figure 3(a). Furthermore, the TWIP–TRIP alloys (13.3 SFE and 13.0 SFE), show no evidence of ε -martensite formation at strains up to 13 pct or greater (see Figure 3) and no evidence of DSA in the tensile tests as shown in Figure 2(b).

Remy and Pineau,^[15] Remy,^[16] and Allain *et al.*,^[17] all stated that ε -martensite will be produced from a stress-induced martensitic reaction if the ISFE \leq 12 mJ/m². They also proposed that a combination of TWIP and ε -martensite will occur when the ISFE is between 12 and 25 mJ/m², calculated according to the model utilized throughout this work, the results of this work are consistent when considering the ISFE of the γ -austenite formed after annealing. Based on the results from Figure 3 and Table IV and using the thermodynamic parameters reported in this work, the γ -austenite with ISFE \geq 11.9 mJ/m² are TWIP–TRIP steels.

As noted in previous studies, the typical flow stress for the γ -austenite to ε -martensite transformation is typically below 300 MPa with γ -austenite grain diameters between 10 and 30 μ m. Microstructural refinement using cold rolling and annealing at 873 K (600 °C) has been shown here to produce yield strengths in excess of 700 MPa when the mean free dislocation path in the polyphase microstructure is reduced below 0.5 μ m. Here it is interesting to compare the intrinsic stacking fault energies and the resultant Hall–Petch parameters

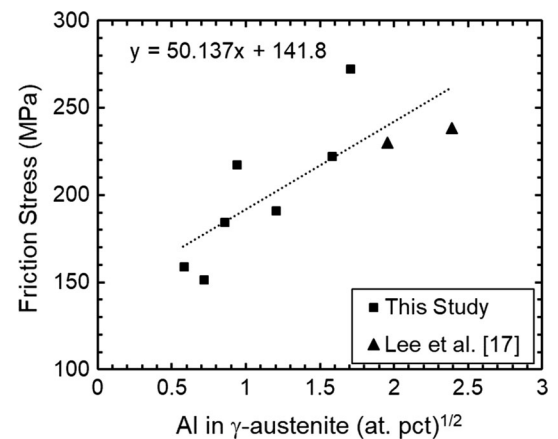


Fig. 14—A regression analysis with linear fit to the friction stress as a function of aluminum concentration (at. pct) to the $\frac{1}{2}$ power for the alloys investigated in this study and the alloys reported by Lee *et al.*^[13] The 13.0 SFE alloy was excluded due to the bimodal grain structure and an exceptionally high calculated friction stress.

for two types of steels: the TWIP–TRIP steel reported by Lee *et al.*^[13] and the two-stage TRIP alloys reported here. An average ISFE of 17.0 mJ/m² was calculated using the same thermodynamic parameters used in the study reported here for the TWIP–TRIP alloys reported by Lee *et al.*, whereas an average of 2.8 mJ/m² was calculated for the alloys of this study. A comparison of Eq. [1] and the least squares fit for the Hall–Petch plot shown in Figure 7 shows two interesting effects of lowering the ISFE: (1) the Hall–Petch grain boundary hardening parameter increases as ISFE decreases and (2) the intrinsic strength or friction stress (y -axis intercept) decreases with decreasing ISFE. Higher values of the Hall–Petch grain boundary hardening term are often associated with lower ISFE in copper alloyed with aluminum as reported by Rohatgi *et al.*^[58] A lower Hall–Petch grain boundary hardening parameter is associated with ease of dislocation cross slip and subsequent stress relaxation of the grain boundary

strained by dislocation pile-ups. Lowering intrinsic stacking fault energy would be expected to reduce cross slip thereby reducing grain boundary stress relaxation and thus produce a higher Hall–Petch grain boundary hardening parameter.

The friction stress of the two-stage TRIP alloys was found to best correlate to the aluminum content of the steel. The friction stress for each alloy was calculated using the average grain boundary strengthening term ($388 \text{ MPa } \mu\text{m}^{1/2}$) and the mean free path measured for each alloy. The calculated friction stress plotted against the $1/2$ power dependence of the aluminum concentration (at. pct) measured according to EDS analysis in the annealed γ -austenite is shown in Figure 14 along with the alloys reported by Lee *et al.*^[13] An increasing friction stress with aluminum content is contrary to what might be expected from first-principle calculations showing that aluminum lowers the unstable stacking fault energy.^[29] Thus, the friction stress is related to the motion of existing defects rather than the nucleation of Shockley partial dislocations. In copper alloys, Rohatgi *et al.* show that the friction stress increases with aluminum addition with a $2/3$ power dependence as expected for higher alloy concentrations.

Friction stresses for the TWIP–TRIP alloys 13.3 SFE and 13.0 SFE were determined to be 272 and 635 MPa. A comparison of the carbon content, 0.09 wt pct for the 13.3 SFE and 0.27 wt pct for the 13.0 SFE, would suggest that carbon plays a more significant role in the friction stress than aluminum. In comparison with the two-stage TRIP alloys of equivalent carbon content, the calculated friction stress for the 13.3 SFE alloy would be 242 MPa based upon aluminum chemistry of the austenite. If the flow stress were directly related to the motion of Shockley partials, then the distinction between TWIP and ϵ -martensite would be the spacing of partial dislocations. As described by Olson and Cohen, twins require Shockley partials on every $\{111\}_\gamma$ plane compared to ϵ -martensite which requires a partial dislocation on alternating $\{111\}_\gamma$ planes.^[41] With fewer required dislocations, it is reasonable to believe that

ϵ -martensite formation in the two-stage TRIP steels would have a lower friction stress compared to the TWIP steels.

Microstructural constituents also have a strong effect on the total ductility of the steel. The product of the volume change for the martensitic transformations and the total volume of the transformable components correlated well with the total ductility of the steels designed to undergo the $\gamma \rightarrow \epsilon \rightarrow \alpha$ TRIP sequence, as shown in Figure 12. Of note, however, are the Batch Annealed 5.0, -2.1 , and -2.2 SFE alloys exhibiting behavior similar to the hot band steels. This effect is tied to an absence of specimen necking during tensile testing as shown in Figure 2 and a low concentration of α -ferrite (< 8 vol pct) in the starting batch-annealed microstructure as shown in Table V. It has been shown that the α -martensite that forms from the strain-induced transformation is hard and brittle,^[13] this brittle α -martensite will not contribute significantly to the total ductility. The three two-stage TRIP alloys containing significant α -ferrite in the starting structure (7.8, -0.2 , and -1.8 SFE) exhibit both post-necking strain and increased ductility; this is potentially a contribution from α -ferrite when the TRIP response is exhausted. Theoretically, the y -intercept of the two equations shown in Figure 12 would be the ductility of the steel without the contributions attributed to TRIP of γ -austenite or ϵ -martensite. In the hot band steels, this is 0.8 pct strain and for freshly formed α -martensite this is a reasonable value. Using a similar argument for the batch-annealed materials, the α -ferrite in the initial microstructure is expected to contribute 19.5 pct strain to the ductility. Both data sets exhibit a similar slope suggesting that the strain contribution from TRIP is equivalent.

Microstructural design of medium manganese steel for enhanced ductility *via* TRIP might suggest that an initial microstructure of ϵ -martensite be preferred, since the volume change to α -martensite is greater than that observed by traditional ($\gamma \rightarrow \alpha$) TRIP. Tensile ductility (Table II) and initial microstructure (Table III) of the

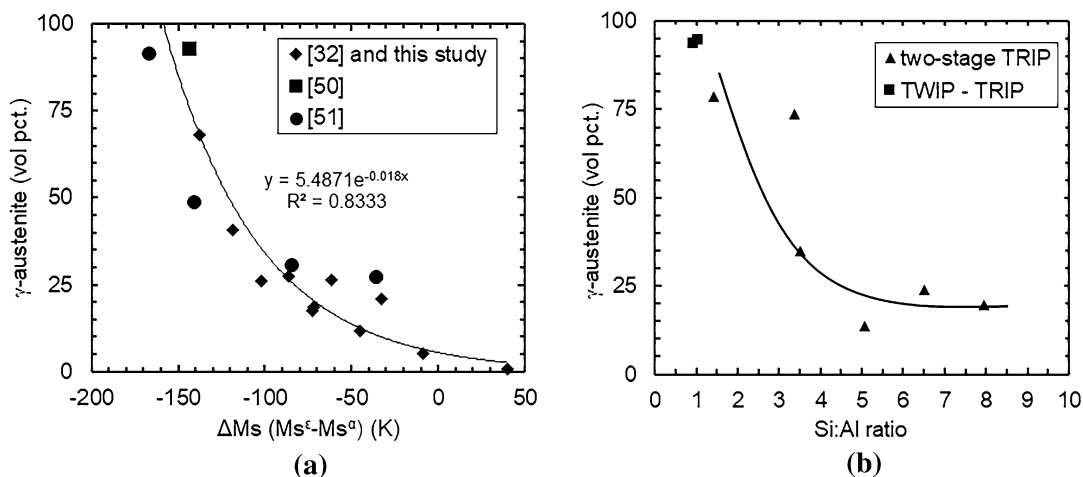


Fig. 15—Measured γ -austenite retained at room temperature for hot rolled medium-Mn steels showing (a) effect of ΔM_s (b) effect of Si:Al ratio with data taken from this study and Ref. [32].

batch-annealed alloys 5.0 SFE and -2.2 SFE support this hypothesis: alloy 5.0 SFE started with 30 vol pct ϵ -martensite and failed at 33.7 pct elongation, whereas the -2.2 SFE alloy had 33 vol pct ϵ -martensite and failed at 27.7 pct elongation. Both alloys produced an austenitic grain structure without α -ferrite, however, neither exhibited necking prior to failure and cleavage fractures were observed. This might suggest that a dual-phase ($\alpha + \gamma$) or a fully austenitic starting microstructure would be preferred.

In a previous study by Field *et al.*, it was shown that the retained austenite content of medium manganese steel was related to the difference in the M_s temperatures ($\Delta M_s = M_s^\epsilon - M_s^\alpha$) for rolled and quenched austenitic microstructures.^[32] For steels exhibiting ϵ -martensite, a more negative ΔM_s correlated to more retained γ -austenite as shown in Figure 15(a). Interestingly, a similar trend can be produced by plotting retained γ -austenite vs Si:Al ratio as shown in Figure 15(b). This unusual correspondence can be explained by noting that aluminum will suppress the M_s^ϵ as shown by Pisarik and Van Aken,^[31] and increases the M_s^α , according to the work by Field *et al.*^[32] In contrast, silicon has a very weak effect on either M_s temperature.^[31,32] Thus, ΔM_s would trend towards a more negative value with increasing aluminum content. This might suggest that correlation to aluminum alone would produce a better fit to the data rather than the ratio of Si:Al; however, this is not observed. It is interesting to speculate that the reduction in retained γ -austenite with increasing Si:Al ratio might also be related to an increase in defect density, which would increase the M_s temperature as a result of larger defect clusters (n). The effect of defect

density on the stability of γ -austenite can be demonstrated in the -2.2 SFE alloy (Si:Al = 3.49) by comparing the hot band, Figure 5(a) and batch annealed, see Figure 6(h) microstructures or the XRD phase quantification in Table III. Additional studies will be required to study this effect in batch-annealed materials.

As noted by Lee *et al.*, an austenitic grain diameter of 200 nm will suppress the M_s temperature of α -martensite by 100 K (100 C°).^[40] The effect of grain size on the M_s^ϵ is not documented as well. Pisarik and Van Aken suggested that a back stress on the dislocation would reduce the width of the stacking fault and this may produce a similar effect where a decrease in the grain size lowers M_s^ϵ .^[31] The mixed grain structure shown in Figure 6(g) of alloy -2.1 SFE may support this inference on grain size; however, banding of α -ferrite formed during intercritical annealing would suggest alloy segregation and differences in manganese content. For γ -austenite grain diameters greater than 30 μm , as observed in the hot rolled 7.8 SFE Figure 9(a) steel a $\Delta M_s = -113$ K (-113 C°) lead to a primarily austenitic microstructure (79 vol pct) with some α -martensite formed upon cooling. Thus, a ΔM_s of less than -100 K is suggested, but a smaller difference may be possible as the grain size is reduced.

In an effort to determine definitively that a starting microstructure of γ -austenite is better than a dual-phase microstructure of either $\gamma + \epsilon$ or $\gamma + \alpha$ two additional alloys were cast and processed in a manner described in the experimental procedure of this paper. Both alloys were formulated to produce properties that met or exceeded the goals set by the Department of Energy for

Table VI. Composition and Calculated Thermodynamic Parameters of the Second Iteration of Two-Stage TRIP Alloys

Alloy	Composition (Weight Percent)							Calculated Parameters*			
	C	Mn	Si	Cr	Al	N	Nb	SFE (mJ/m ²)	M_s^ϵ K (C°)	M_s^α K (C°)	ΔM_s (C°)
Cr	0.16	13.9	1.1	3.3	0.03	0.016	0.042	-0.9	376 (103)	493 (219)	-116
Cr + Al	0.17	14.0	1.2	3.2	1.6	0.033	0.051	10.6	269 (-4)	505 (232)	-236

*Values calculated for a single-phase γ -austenite.

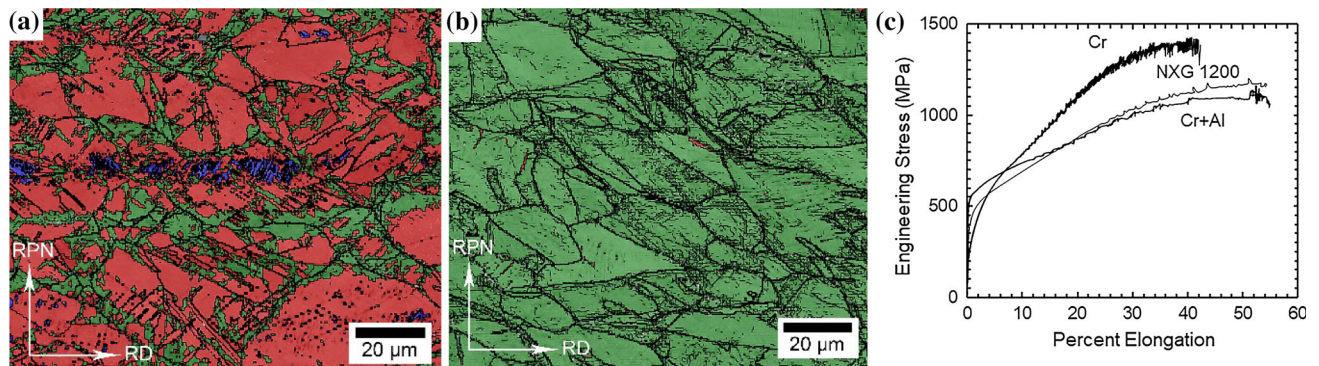


Fig. 16—EBSD phase maps of the hot band (a) Cr alloy, (b) Cr + Al alloy, and (c) tensile response of the hot band two-stage TRIP alloys with the NXG™ 1200 alloy for comparison. Austenite is shown in green, ϵ -martensite is red, and the α -martensite is blue (Color figure online).

Table VII. Composition and Calculated Thermodynamic Parameters of the γ -Austenite from Multiphase Equilibria Simulation Using FactSage

Alloy	γ -austenite						Carbides (Weight Percent)				
	Composition (Weight Percent)						SFE (mJ/m ²)	Ms ^e K (°C)	Ms ^a K (°C)	M ₂₃ (C,N) ₆	NbC
	C	Mn	Si	Cr	Al	N					
Cr	0.06	13.8	1.1	2.5	—	0.005	− 4.6	400 (127)	416 (143)	1.78	0.076
Cr + Al	0.07	13.9	1.2	2.3	1.5	< 0.001	6.6	301 (28)	441 (168)	1.81	0.048

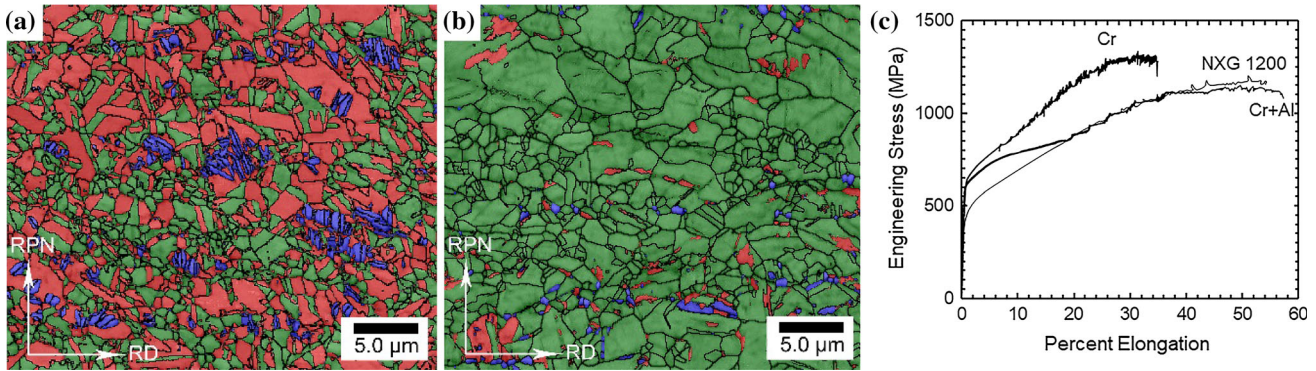


Fig. 17—EBSD phase maps of the cold worked and annealed (a) Cr alloy, (b) Cr + Al alloy, and (c) tensile response of the cold worked and annealed two-stage TRIP alloys with the NXGTM 1200 alloy for comparison. Austenite is shown in green, ϵ -martensite is red, and the α -martensite is blue (Color figure online).

Table VIII. Measured and Calculated Tensile Properties. Calculated Yield Strength Based on Mean Free Microstructural Path (L_3) and Figure 7 Line Fit. Calculated Ultimate Tensile Strength and Percent Elongation to Failure Using γ -Austenite Composition and Eqs. [7] & [8] with the Percent Relative Errors Given

Alloy	Measured Properties						Calculated Properties		
	Hot Band			Batch Annealed			Batch Annealed		
	YS (MPa)	UTS (MPa)	e_f (Percent)	YS (MPa)	UTS (MPa)	e_f (Percent)	YS* (MPa) [Pct Error]	UTS [#] (MPa) [Percent Error]	e_f [#] (percent) [Percent Error]
Cr	232	1390	42.6	660	1330	35.0	625 [− 5.3]	1260 [− 5.2]	35.5 [1.4]
Cr + Al	523	1140	53.6	540	1150	58.8	500 [− 7.4]	1200 [4.3]	63.3 [7.7]

*Yield strength is calculated according to the measured grain size.

[#]Ultimate tensile strength and elongation to failure are calculated from the composition-based equations from Eqs. [7] and [8].

3rd generation advanced high-strength steels using Eqs. [7] and [8]. The alloys were also formulated to give a ΔMs of less than -100 K (100 C°). The composition, bulk ISFE, and Ms temperatures are listed in Table VI. Silicon content was reduced to ~ 1 wt pct to improve recovery and recrystallization in the hot band condition. Chromium was added in sufficient quantity to produce M₂₃(C,N)₆ precipitation and thus mitigate dynamic strain aging associated with interstitials. One steel was also alloyed with aluminum to investigate if the elevated ISFE of 10.6 mJ/m² would produce the two-stage TRIP response. These alloys are designated Cr and Cr + Al.

The hot band microstructures and tensile properties of the Cr and the Cr + Al alloys are shown in Figure 16 along with tensile results from the NXGTM1200 steel produced by AKSteel and NanoSteel.^[59] It is noted that the Cr alloy contains a significant volume fraction of ϵ -martensite (47 vol pct) and this is understood to be due to the elevated Ms^e temperature (376 K). The Cr alloy also exhibits continuous DSA over the entire strain range of the tensile test, whereas the Cr + Al begins to show DSA at the start of the tensile curve inflection in a similar fashion to the NXGTM1200 steel. The greater magnitude of the ΔMs calculated for the Cr + Al

compared to the Cr alloy is expressed in a primarily austenitic structure after hot rolling (98 vol pct). After cold rolling and annealing at 923 K (650 °C) for 20 hours, the precipitation of the $M_{23}(C,N)_6$ and NbC is calculated using the FactSage thermodynamic software package, using the FSstel database, and the ISFE of the γ -austenite is altered from the single-phase composition value as calculated in Table VI. Specifically, the Cr, C, and N contents are reduced and the volume fraction of carbides and the ISFE of the γ -austenite is recalculated utilizing the multiphase equilibria from FactSage with the values shown in Table VII. Precipitation of $M_{23}(C,N)_6$ during annealing produces a lower ISFE and increases the ε -martensite start temperature in each alloy, which is most significant for the Cr + Al alloy that now shows ε -martensite in the annealed microstructure. Both $M_{23}(C,N)_6$ and NbC have been verified in alloys containing Cr and Nb and these results will be reported elsewhere.

Tensile properties and microstructure of the cold rolled and annealed alloys are shown in Figure 17 and Table VIII shows a comparison of the predicted tensile properties using the grain size and the γ -austenite phase composition for the batch-annealed steels. Mean free slip distances of 0.8 μm and 1.5 μm were measured for the Cr and Cr + Al alloys. The tensile response of the Cr + Al alloy is little changed from the hot band condition and shows remarkable similarity to the NXGTM1200 steel. A significant increase in yield strength is demonstrated in the Cr alloy and this is attributed to the significant reduction in grain size from the hot band condition. Based upon these findings, it may be concluded that a predominately austenitic microstructure will yield the best combination of strength and ductility when a two-stage TRIP response is achieved.

V. SUMMARY

A methodology for designing two-stage TRIP alloys has been presented using thermodynamic calculations of intrinsic stacking fault energy and martensite start temperatures for both ε and α martensites. Ideally, the start temperature for ε -martensite is kept near ambient temperature with the α -martensite temperature being 100 to 200 K greater than that of the ε -martensite to maximize γ -austenite in the starting microstructure. Chromium should be added in sufficient quantity and precipitated as $M_{23}(C,N)_6$ during the 600 °C anneal to mitigate dynamic strain aging associated with interstitial carbon in γ -austenite or nitrogen in α -ferrite as shown previously by the authors in reference 21. Aluminum, silicon, and manganese additions are balanced to encourage the following: (1) recrystallization during thermomechanical processing to produce an equiaxed austenite grain size on the order of 1–2 μm , *i.e.*, Si:Al=1.0, (2) addition of aluminum to increase solid solution strengthening of α -ferrite if produced by intercritical annealing, (3) an γ -austenite composition after the 600 °C anneal with an intrinsic stacking fault energy for two-stage TRIP, *i.e.*, ISFE $\leq 10.5 \text{ mJ/m}^2$, and

(4) the requisite martensite start temperatures to maximize the γ -austenite content in the steel that leads to a two-stage TRIP response. Total ductility was correlated to the product of the volume change and the total volume percent of the TRIP components in the starting microstructure for the two-stage TRIP steels in both the hot band and batch-annealed condition. Design of two-stage TRIP steels using intrinsic stacking fault energy and martensite start temperatures determined from austenite chemistry has proven to be a reliable method of producing steels with the required properties as defined by the department of energy for future 3rd generation advanced high-strength steels.

ACKNOWLEDGMENTS

This work was supported by the Peaslee Steel Manufacturing Research Center (PSMRC). Companies directly involved in this work include AK Steel, ArcelorMittal, Nucor Steel, and U. S. Steel. The FEI Helios NanoLab dual beam FIB was obtained with a Major Research Instrumentation Grant from the National Science Foundation under Contract DMR-0723128. The FEI Tecnai F20 scanning/transmission electron microscope was obtained through a major research instrumentation Grant from the National Science Foundation under Contract DMR-0922851. The authors also acknowledge the support of the Materials Research Center and in particular Dr. Clarissa Wisner for training on the SEM as well as Dr. Eric Bohannon for performing the XRD work. Special thanks are also extended to Dr. Narayan Pottore and Dr. Bernard Chukwulebe at ArcelorMittal, Todd Link from U.S. Steel, Eric Gallo at Nucor, and Dr. Luis Garza from AK Steel for their discussion and guidance on the engineering requirements for future 3rd generation advanced high-strength steels.

REFERENCES

1. Q. Li, X. Huang, and W. Huang: *Met Sci. Eng.*, 2016, vol. 662, pp. 129–35.
2. E.J. Seo, L.C.Y. Estrin, and B.C. De Cooman: *Acta Mater.*, 2016, vol. 113, pp. 124–39.
3. L. Cho, E.J. Seo, and B.C. De Cooman: *Scr. Mater.*, 2016, vol. 123, pp. 69–72.
4. T. Tschiyama, T. Inoe, J. Tobata, D. Akami, and S. Takaki: *Scr. Mater.*, 2016, vol. 122, pp. 36–39.
5. D.-W. Suh, S.-J. Park, T.-H. Lee, C.-S. Oh, and S.-J. Kim: *Met Trans A*, 2010, vol. 41A, pp. 397–408.
6. D.-W. Suh, J.-H. Ryu, M.-S. Joo, H.-S. Yang, H.K.D.H. Bhadeshia: *Met Trans A*, 2013, vol. 44A, pp. 286–93.
7. J. Shi, X. Sun, M. Wang, W. Hui, H. Dong, and W. Cao: *Scr. Mater.*, 2010, vol. 63, pp. 815–18.
8. Z.H. Cai, H. Ding, R.D. Misra, and Z.Y. Ying: *Acta Mater.*, 2015, vol. 84, pp. 229–36.
9. R. Zhang, W.Q. Ca, Z.J. Peng, J. Shi, H. Dong, and C.X. Huang: *Mater. Sci. & Eng. A*, 2013, vol. 583, pp. 84–88.
10. R. Skolly, ArcelorMittal personal communication.
11. Y. Zhang, L. Wang, K.O. Findley, and J. Speer: *Met Trans. A*, 2017, vol. 48A, pp. 2140–49.

12. H. Luo, H. Dong, and M. Huang: *Mater. & Des.*, 2015, vol. 83, pp. 42–48.
13. S. Lee, W. Woo, and B.C. De Cooman: *Met. Trans. A*, 2016, vol. 47A, pp. 2125–40.
14. G. Frommeyer, U. Brux, and P. Neumann: *ISJ Inter.*, 2003, vol. 43, pp. 438–46.
15. L. Remy and A. Pineau: *Mater. Sci. Eng.*, 1976, vol. 26, pp. 123–32.
16. S. Allain, J.P. Chateau, and O. Bouaziz: *Mater. Sci. Eng.*, 2004, vol. 387, pp. 143–47.
17. T.H. Lee, E. Shin, C.S. Oh, H.Y. Ha, and S.J. Kim: *Acta Mater.*, 2010, vol. 58, pp. 3173–86.
18. H. Song, S.S. Sohn, J.-H. Kwak, B.-J. Lee, and S. Lee: *Met. Trans. A*, 2016, vol. 47A, pp. 2674–85.
19. O. Grässel, L. Krüger, G. Frommeyer, and L.W. Meyer: *Int. J. Plast.*, 2000, vol. 16, pp. 1391–1409.
20. B.C. De Cooman, P. Gibbs, S. Lee, and D.K. Matlock: *Met. Trans. A*, 2013, vol. 44A, pp. 2563–72.
21. D.M. Field and D.C. Van Aken: *Metall. Mater. Trans. A*, 2018, vol. 49A, pp. 1152–66.
22. S.T. Pisarik, D.C. Van Aken, K. Limmer, and J.E. Medvedeva: *AISTech 2014 Proceedings*, 2014, vol. III, pp. 3013–23.
23. S.K. Huang, Y.H. Wen, N. Li, J. Teng, S. Ding, and Y.G. Xu: *Mater. Charact.*, 2008, vol. 59, pp. 681–87.
24. S. Shin, M. Kwon, W. Cho, I.S. Suh, and B.C. De Cooman: *Mater. Sci. & Eng.*, 2017, vol. 683, pp. 187–94.
25. M.C. McGrath, D.C. Van Aken, N.I. Medvedeva, and J.E. Medvedeva: *Metall. Mater. Trans. A*, 2013, vol. 44A, pp. 4634–43.
26. X.-S. Yang, S. Sun, H.-H. Ruan, S.-Q. Shi, and T.-Y. Zhang: *Acta Mater.*, 2017, vol. 136, pp. 347–54.
27. D.C. Van Aken, S.T. Pisarik, and M.C. McGrath: *Proceedings of the International Symposium on New Developments in Advanced High-Strength Steels*, Vail, Colorado, 2013, pp. 119–29.
28. D.M. Field and D.C. Van Aken: *Met. Trans. A.*, 2016, vol. 47A, pp. 1912–17.
29. N.I. Medvedeva, M.S. Park, D.C. Van Aken, and J.E. Medvedeva: *J. Alloys Compd.*, Vol. 582, 2014, pp. 475–82.
30. K.R. Limmer, J.E. Medvedeva, D.C. Van Aken, and N.I. Medvedeva: *Comput. Mater. Sci.*, 2015, vol. 99, pp. 253–55.
31. S.T. Pisarik and D.C. Van Aken: *Met. Trans. A.*, 2016, vol. 47A, pp. 1009–1018.
32. D.M. Field, D.S. Baker, and D.C. Van Aken: *Metall. Mater. Trans. A*, 2017, vol. 48A, pp. 2150–63.
33. P.P. Suikkanen, V.T.E. Lang, M.C. Somani, D.A. Prter, and L.P. Karjalainen: *ISIJ Int.*, 2012, vol. 52, pp. 471–76.
34. Z. Li-Juan, W. Di, and Z. Xian-ming: *J. Iron Steel Res. Int.*, 2007, vol. 14, pp. 61–65.
35. L.J. Zhu, D. Wu, and X.M. Zhao: *Acta Metall.*, 2008, vol. 21, pp. 163–68.
36. M.C. Somani, L.P. Karjalainen, D.A. Porter, and R.A. Morgridge: *Proceedings of International Conference on Thermo-mechanical Processing Mechanics: Microstructures and Controls*, University of Sheffield, Sheffield GB, (2003), 436.
37. S.F. Medina and J.E. Mancilla: *ISIJ Int.*, 1996, vol. 36, pp. 1036–1070.
38. S.F. Medina and A. Quispe: *ISIJ Int.*, 2001, vol. 41, pp. 774–80.
39. S.-J. Lee, J. Kim, S.N. Kane, and B.C. De Cooman: *Acta Mater.*, 2011, vol. 59, pp. 6809–19.
40. S.J. Lee, S.W. Lee, and B.C. De Cooman: *Int. J. Mater. Res.*, 2013, vol. 104, pp. 423–29.
41. G.B. Olson and M. Cohen: *Met. Trans. A*, 1976, vol. 7, pp. 1897–1904.
42. ASTM E 8/E 8M-08, Standard Test Methods for Tension Testing of Metallic Materials.
43. S. Martin, C. Ullrich, D. Simek, U. Martin, and D. Rafaja: *J. Appl. Crystallogr.*, 2011, vol. 44, pp. 779–87.
44. N. Stanford and D.P. Dunne: *Acta Mater.*, 2010, vol. 58, pp. 6752–62.
45. S.T. Pisarik and D.C. Van Aken: *Met. Trans. A.*, 2014, vol. 45, pp. 3173–78.
46. M. Papa Rao, V. Subramanya Sarma, and S. Sankaran: *Met. Trans. A* 2014, vol. 45A, pp. 5313–17.
47. M. Papa Rao, V. Subramanya Sarma, and S. Sankaran: *Mater. Sci. & Eng. A* 2013, vol. 568, pp. 171–75.
48. O. Saray, G. Purcek, I. Karaman, and H. Maier: *Met. Trans. A*, 2012, vol. 43A, pp. 4320–30.
49. V.S.A. Challa, R.D.K. Misra, M.C. Comani, and Z.D. Wang: *Mater. Sci. Eng.*, 2016, vol. 661, pp. 51–60.
50. Y. Son, Y.K. Lee, K.-T. Park, C. S. Lee, and D. H. Shin: *Acta Mater.* 2005, vol. 53, pp. 3125–34.
51. M. Calcagnotto, Y. Adachi, D. Ponge, and D. Raabe: *Acta Mater.* 2011, vol. 59, pp. 658–70.
52. D.H. Shin and K.-T. Park: *Mater. Sci. Eng. A*, 2005, vols. 410–411, pp. 299–302.
53. M. Calcagnotto, D. Ponge, E. Demir, and D. Raabe: *Mater. Sci. Eng. A*, 2010, vol. 527, pp. 2738–46.
54. R.D.K. Misra, P.K.C. Vankatsurya, M.C. Somani, and L.P. Karjalainen: *Met. Trans. A*, 2012, vol. 43A, pp. 5286–97.
55. P.J. Gibbs, E. De Moor, M.J. Merwin, B. Clausen, J.G. Speer, and D.K. Matlock: *Met. Trans. A*, 2011, vol. 42A, pp. 3691–3701.
56. G. Dini, A. Najafzadeh, R. Ueji, and S.M. Monir-Vaghefi: *Mater. Lett.*, 2010, vol. 64, pp. 15–18.
57. S. Rajasekhara, P.J. Ferreira, L.P. Karjalainen, and A. Kyröläinen: *Met. Trans. A.*, 2007, vol. 38A, pp. 1202–10.
58. A. Rohatgi, K.S., Vecchio, and G.T. Gray III: *Met. Trans. A*, 2001, vol. 32A, pp. 135–45.
59. D.J. Branagan, C.S. Parsons, T.V. Machrowicz, A.E. Frerichs, B.E. Meacham, S. Cheng, and A.V. Sergueeva 2016, *Launch of a New Class of 3rd Generation Cold Formable AHSS* [PowerPoint slide 15 & 16].